Design of a Robust Radio Frequency Fingerprint Identification Scheme for Multi-Mode LFM Radar

Yuexiu Xing, Aiqun Hu, Junqing Zhang, Jiabao Yu, Guyue Li, and Ting Wang

***Abstract*—Radar is an indispensable part of the Internet of Things (IoT). Specific emitter identification is essential to identify the legitimate radars and, more importantly, to reject the malicious radars. Conventional methods rely on pulse parameters that are not capable to identify the specific emitter as two radars may have the same configuration or a malicious radar can perform spoofing attacks. Radio frequency fingerprint (RFF) is the unique and intrinsic hardware characteristic of devices resulted from hardware imperfection, which can be used as the device identity. This paper proposes a robust and reliable radar identification scheme based on the RFF, taking linear frequency modulation (LFM) radar as a case study. This scheme first classifies the operation mode of the pulses, then eliminates the noise effect, and finally identifies the radar emitters based on the transient and modulation-based RFF features. Experimental results verify the effectiveness of our radar identification scheme among three real LFM radars (same model) operating at four modes, each mode with 2,000 pulses from each radar. The identification rates of the four modes are all higher than 90% when the signal-to-noise ratio (SNR) is about 5 dB. In addition, mode 3 achieves almost 100% identification accuracy even when the SNR is as low as -10 dB.**

***Index Terms*—Radio frequency fingerprint, multi-mode radar, linear frequency modulation, denoising, radar identification**

I. Introduction

RADAR is widely used for object detection and navigation [1]. It is an indispensable part of the Internet of Things (IoT). Radar has intrigued many exciting applications such as motion compensation and autonomous navigation for unmanned aerial vehicle (UAV) [2], hand gesture recognition [3], vehicle positioning [4], human sense system [5]–[7]. Same as other IoT techniques, the radar emitter identification is essential against replay, man-in-the-middle (MITM), denial of service (DoS), IP or MAC spoofing [8]–[12]. Classic radar identification schemes classify radars by pulse parameters, such as repetition intervals [13]. However, radar systems can typically exhibit very similar electromagnetic characteristics, especially under the same configuration [14]. Thus, pulse parameters are usually not sufficient to identify a specific emitter and anti-spoofing. Therefore, a robust radar emitters identification technique is strongly required.

Radio frequency fingerprint (RFF) identification is an emerging device identification solution, which leverages the hardware imperfections resulting from the manufacturing process [15]. The expression of RFF features is slight distortions of the transmitted signal, such as inphase/quadrature (I/Q) mismatch, which is unique and difficult to tamper with [16]. Radar emitters also have inevitable hardware imperfections, hence RFF identification can be a potential solution for classifying radar emitters. There are three particular design considerations when RFF is applied for radar emitters identification, namely the effects of modulation parameters on the RFF, the low signal-to-noise ratio (SNR) situations of radar applications, and the RFF feature extraction method of the radar pulse.

RFF extraction will be directly affected by the modulation configurations [17]–[20]. The signal bandwidth has been found to have a significant impact on the identification performance [19], [20]. For example, Andrews *et al.* configured 53 universal software radio peripheral (USRP) platforms with 11 bandwidths and demonstrated the RFF feature spaces were totally different [19]. Radar can operate at different modes with various carrier frequencies and bandwidths. D'Agostino *et al.* explored the identification of real radar in three modes with different carrier frequencies [17], [18]. Their results showed that the RFF features were not robust with respect to the radar mode. It is thus necessary to classify the input radar pulses into different sets based on modulation parameters before extracting the RFF features. However, a practical radar mode classification algorithm is currently missing in RFF-based radar identification approaches.

Low received SNR is quite common in many radar applications, such as satellite remote sensing and vehicle radars. Noise will greatly reduce the identification accuracy [21]–[23]. Hence, noise reduction without impacting the RFF features is demanding, which has been investigated in [24]–[28]. Xing *et*

Manuscript received January 9, 2020; revised May 6, 2020; accepted June 16, 2020. Date of publication xx, 2020; date of current version xx, 2020. This paper was presented in part at the 15th International Conference on Wireless and Mobile Computing, Networking and Communications, Barcelona, Spain, October 2019. This work was supported in part by Research Fund of National Mobile Communications Research Laboratory, Southeast University (No.2020B05), Jiangsu Provincial Key Research and Development Program (BE2019109), National Natural Science Foundation of China (61571110, 61801115, 61941115), Purple Mountain Laboratories for Network and Communication Security, Campus France PHC Cai Yuanpei 2019 project (44016XA), and China Scholarship Council. The work of J. Zhang was supported by Royal Society Research Grants under grant ID RGS/R1/191241. (*Corresponding author: A. Hu.*)

Y. Xing, A. Hu and J. Yu are with the School of Information Science and Engineering, Southeast University, 210096 Nanjing, China. (e-mail: {yxxing, aqhu, yujiabao}@seu.edu.cn).

J. Zhang is with the Department of Electrical Engineering and Electronics, University of Liverpool, Liverpool, L69 3GJ, United Kingdom. (email: junqing.zhang@liverpool.ac.uk).

G. Li is with School of Cyber Science and Engineering, Southeast University, 210096 Nanjing, China. (e-mail: guyuelee@seu.edu.cn).

T. Wang is with the LIGM lab, University of Gustave Eiffel, CNRS, ESIEE Paris, Marne-la-Vallée, France. (email: ting.wang@esiee.fr).

A. Hu, J. Yu, and G. Li, A are also with the Purple Mountain Laboratories for Network and Communication Security, Nanjing, 210096, China.

Digital Object Identifier xxx

al. proposed an information data estimation-based stacking algorithm, which leverages the repeated sequences and stacks them together to reduce the noise [26]. Similarly, the optimized coherent integration based denoising algorithm in [27] also improved SNR by adding and integrating multiple signals. However, both methods rely on multiple repetitive signals, which is not suitable for the radar identification that uses single pulse. Yu *et al.* designed a denoising autoencoder-based model for extracting deep features of the signal [28]. The model requires a clean data-set corresponding to the training set, which is difficult to obtain. A novel denoising algorithm for RFF-based radar identification is thus urgently needed, which should be performed in one pulse and not require any extra information.

RFF can be extracted from the transient signals (transient-based RFF) and/or the steady-state signals (modulation-based RFF) [29]. First of all, transient signals and steady-state signals are readily available in radar systems. In addition, the radar equipment is high-sensitivity, which means it is sufficient to capture transient signals [22], [30]. Therefore, a hybrid RFF identification method including both transient-based RFF and modulation-based RFF for radar can be designed, which should be superior to use only one kind of RFF feature.

In summary, RFF identification for radar operating at multi-mode and low SNR conditions is challenging. Linear frequency modulation (LFM)-based radar is widely used because of its excellent detection capability, range resolution and relatively simple hardware architecture [31], [32]. This paper takes the LFM radar as an example to investigate these challenges. The main contributions are summarized as follows.

- We design a dynamic and self-refining classification (DRC) algorithm for radar operation mode classification. This algorithm can dynamically establish and update operation mode library, and clear the interference pulses by periodically refining the library. The results show that the algorithm has excellent pulse classification performance and interference pulse removal ability.
- Inspired by the classical three parameter sine wave curve-fit algorithm [33], we propose a piecewise curve fitting based denoising (PCFD) algorithm for noise suppression. It preserves RFF information effectively while reduces the noise dramatically. This algorithm brings 50% identification accuracy improvement when the SNR is -5 dB.
- We propose a hybrid RFF identification method, which can extract both transient-based and modulation-based RFF features. The signal derivation and envelope operations make RFF features in the signal more prominent and easy to extract, which is effective for LFM signal identification.
- We verify the effectiveness of the proposed scheme on three real radars spanning four operation modes with 6,000 pulses per mode. Experimental results show that the identification accuracy for four operation modes all exceeds 90%, when SNR is about 5 dB. For Mode 3, the identification rate can reach about 100% even at -10 dB.

Our previous work proposed the PCFD algorithm and the hybrid RFF identification algorithm for LFM radars in single mode [34]. This paper considerably extended and complemented our previous work by investigating RFF-based radar identification with multiple modes. Furthermore, we conducted more comprehensive experiments in four modes of three real radars (24,000 pulses in total) to evaluate our approach.

The rest of this paper is organized as follows. Section II reviews the related work. Section III introduces the system model. Section IV and Section V present our mode classification algorithm and denoising algorithm, respectively. Section VI describes the hybrid RFF identification algorithm. Section VII shows the performance evaluation of the proposed scheme. Finally, Section VIII concludes the paper.

II. Related Work

Classic radar identification describes a radar using the so-called pulse descriptor word (PDW), which includes pulse repetition interval, angle of arrival, pulse width, etc [14]. It aims to determine the number of present radar emitters and classify incoming pulses according to emitters. However, in modem radar systems, more sophisticated signal waveforms have been adopted and using PDW only may not be sufficient to separate those received pulses [14]. Then, intrapulse modulation features are used to further improve the radar identification capability. Liu *et al*. presented a time-frequency analysis based method to identify four typical modulations in the radar signal [35]. Similarly, Guo *et al.* designed a scheme based on the main ridge slice of ambiguity function to identify six modulations of radar signals [36]. However, there are scenarios where the radar modulations are the same, which results in the identification of a specific radar impossible.

RFF is a promising identification solution for devices with exactly the same parameters and modulations, which has been investigated in various wireless systems, such as ZigBee [37], WiFi [38], RFID [39], etc. Deep learning has been demonstrated to be effective in RFF and signal recognition [40]–[43]. The convolutional neural network (CNN)-based methods are employed for automatic modulation recognition, which achieved a good classification capability [41], [42]. Yu *et al.* exhibited a good RFF identification performance for ZigBee devices with a multi-sampling convolutional neural network (MSCNN) [43]. However, deep learning-based methods require a large amount of training data sets and need retraining whenever a new device is added. It is computationally intensive and difficult to achieve in some scenarios, such as identifying non-cooperative devices.

Other existing RFF technologies can be divided into transient-based and modulation-based RFF methods. Transient-based RFF is extracted from turn-on/off signals [25], [44]. Dong *et al.* simulated four kinds of radar pulses and achieved 98.8% identification accuracy by extracting the transient signal envelopes as RFF [45]. However, the modeling of the simulated transient signal is empirical, which may not match the actual pulse accurately. Modulation-based RFF methods focus on steady-state signals, which includes abundant RFF features, such as frequency offset [23] and amplifier non-linearity [46]. For radar identification, Świercz *et al.* utilized the wavelet transform to identify radars

and attain a 100% classification accuracy [21]. However, this simulation work only considered different slopes in steady-state signal as the RFF features but did not involve any real data. Aubry *et al.* extracted pulse's cumulants as the RFF features from the steady-state part of the pulse [47]. However, not all types of radars meet their assumptions (the signal is a zero-mean discrete time complex stationary stationary random process), such as LFM radars. In addition, the operation mode recognition is also a key part in the radar RFF identification. D'Agostino *et al.* explored the specific radar identification with three different operation modes [17], [18]. However, the number of experimental pulses in each mode is only 20.

This paper aims to bridge the above gaps by proposing a robust RFF identification scheme for LFM radars that operate under multi-mode and low SNR conditions. The performance will be validated by extensive experimental data.

III. System overview

Besides its adoption in radar, LFM is also commonly used in the field of IoT, namely LoRa [48], and sonar [49]. A LFM pulse with a normalized amplitude during the interval of $[0, T]$ can be written as

$$s^{RF}(t) = \exp(j2\pi(f + 0.5\mu t)t + \varphi)\exp(j2\pi f^c t) + Z^{RF}(t), \quad 0 \le t \le T, \tag{1}$$

where f, μ, φ, f^c, T represent the initial frequency, chirp rate, initial phase, carrier frequency and pulse width of the received pulse, respectively, $Z^{RF}(t)$ is the additive white Gaussian noise (AWGN) with zero mean and variance σ^2. The initial phase φ is random and non-configurable in a real radar system. A LFM pulse is thus actually determined by four modulation parameters, namely f, μ, f^c, T.

In the real hardware, each of the above parameter consists of the ideal value and the deviation, which can be given as

$$f = f_0 + f_F, \tag{2}$$

$$\mu = \mu_0 + \mu_F, \tag{3}$$

$$f^c = f_0^c + f_F^c, \tag{4}$$

$$T = T_0 + T_F, \tag{5}$$

where the subscripts $(\cdot)_0$ and $(\cdot)_F$ denote the ideal value and deviated feature of the parameter, respectively. The deviation is resulted from the manufacturing imperfection and cannot be entirely eliminated, which is the RFF that we aim to extract.

The configured ideal parameters of the considered radar dataset are given in Table I. Each setup is termed as an operation mode of the radar. When the radar is configured with a specific mode, it will affect the hardware features. For example, the bandwidth of the LFM signal can be given as

$$BW = \mu T. \tag{6}$$

The varying bandwidth will affect the residing RFF features.

A robust RFF-based identification scheme for multi-mode LFM pulse radars is thus designed, which includes three parts and illustrated in Fig. 1. A DRC algorithm will first classify the operation modes of the received pulses. Since the initial frequency f and carrier frequency f^c cannot be estimated separately at the receiver without prior information, their sum f^e is estimated instead. Thus, the following three parameters,

$$\mathbf{\Theta} = [f^e, \mu, T], \tag{7}$$

are used for operation mode classification. The second part is the denoising algorithm named PCFD, which provides SNR-enhanced pulses for the hybrid RFF identification module while keeping the RFF features intact. Finally, a hybrid RFF identification algorithm is proposed including both transient-based and modulation-based RFF features. Their details will be explained in Section IV, V and VI, respectively.

TABLE I
Radar Operation Mode.

Mode	f_0 (MHz)	μ_0 (MHz/μs)	T_0 (μs)	f_0^c (MHz)
Mode 1	0	2/100	100	255
Mode 2	0	2/300	300	255
Mode 3	0	4/100	100	255
Mode 4	0	4/300	300	255

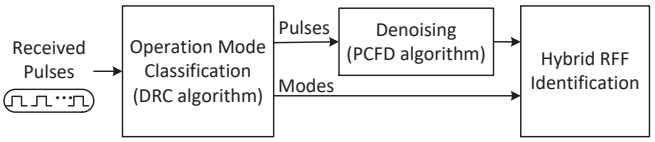

Fig. 1. System model of the RFF-based identification scheme.

IV. Operation mode classification using DRC

RFF features are always related to the signal forms [15], [17]. Pulses with different modulation parameters, such as the pulse width, may have different dimensions of RFF feature vector and affect the RFF identification. Hence, it is necessary to classify the received LFM pulses into different operation modes before extracting the RFF features. Thus, we designed an operation mode classification algorithm named DRC, which can not only dynamically establish and update operation mode library, but also periodically refine the library (clear the interference pulses). The flow chart is illustrated in Fig. 2 and the detailed process is given in Algorithm 1.

A. Pulse Parameter Estimation

When receiving the i-th LFM pulse $s_i^{RF}(t)$, we estimate its parameters, $\mathbf{\Theta}_i = [f_i^e, \mu_i, T_i]$, in line 4 of Algorithm 1. f_i^e and μ_i can be calculated by fast Fourier transform (FFT) and fractional Fourier transform (FrFT) algorithms [50], respectively.

Regarding T_i, it can be obtained by searching the start and end points of the signal based on the signal amplitude. However, since the LFM signal is an oscillating waveform, a plurality of points will be obtained when detecting the amplitude of the original signal, which means the pulse width cannot be accurately detected. Therefore, we first detect the envelope of the received pulse as

$$\widetilde{s_i^{RF}}(t) = |s_i^{RF}(t)|, \tag{8}$$

where $|\cdot|$ means taking the absolute value. Then, we normalize it and find two sampling points with amplitude 0.5 (-6 dB) on

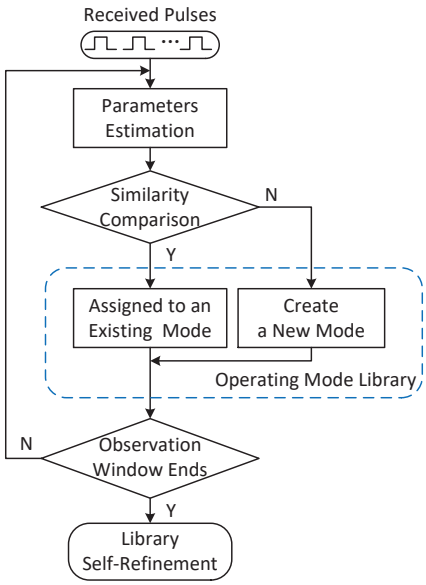

Fig. 2. Flow chart of the mode classification algorithm (DRC algorithm).

the normalized envelope $\widetilde{s_i^{RF}}(t)$, which are t_i^1 and t_i^2. They are the arrival time of pulse rising edge and pulse falling edge, respectively. T_i can then be given as

$$T_i = t_i^2 - t_i^1. \tag{9}$$

B. Operation Mode Classification

Before the first pulse arrives ($i = 1$), the library is empty. We thus create the first operation mode $\mathbb{M}_1$ and push the pulse signal $s_1^{RF}(t)$ and its parameters $\mathbf{\Theta}_1$ into it, $\mathbb{M}_1 = \{[s_1^{RF}(t)], [\mathbf{\Theta}_1]\}$, as shown in line 7.

When a new pulse is detected, i.e., $i \neq 1$, based on the similarity comparison, the pulse will be assigned to an existing mode or a new mode will be created.

The similarity comparison is carried out by comparing normalized $\mathbf{\Theta}_i$ with all existing operation modes in the library $\mathbb{L}$, which can be mathematically given as

$$D(n) = \overline{ED}(\mathbf{\Theta}_i, \mathbb{M}_n\{\mathbf{\Theta}\}), n = 1, 2, \cdots, N_m \tag{10}$$

where $\mathbb{M}_n\{\mathbf{\Theta}\}$ is the pulse parameter set of n-th mode $\mathbb{M}_n$, $\overline{ED}(\cdot,\cdot)$ represents the mean of the Euclidean distance between the one sample and all samples in a set, N_m denotes the number of existing operation modes. Afterward, we can find out the closest mode by

$$\begin{aligned} I^{\min} &= \arg\min_n D(n), \\ D^{\min} &= D(I^{\min}), \end{aligned} \tag{11}$$

where $I^{\min}$ is the corresponding index to $D^{\min}$, as given in line 11. When $D^{\min} < \gamma$, the pulse $s_i^{RF}(t)$ and its parameters $\mathbf{\Theta}_i$ should be put into the existing mode $\mathbb{M}_{I^{\min}}$. Otherwise, a new operation mode, $\mathbb{M}_{N_m+1} = \{[s_i^{RF}(t)], [\mathbf{\Theta}_i]\}$, should be created.

The threshold γ should satisfy

$$\gamma_p < \gamma < \gamma_m, \tag{12}$$

Algorithm 1 DRC algorithm

Input:
$s_i^{RF}(t)$, The LFM pulse signal;
γ, The distance threshold;
N_w, The length of observation window;
λ, The threshold of deleting interference pulse mode.
Output:
Operation mode library $\mathbb{L}$.
{*Initialization*}
1: Set pulse index $i = 0$;
2: Set number of modes $N_m = 0$;
{*Mode Classification*}
3: **while** $s_i^{RF}(t) \neq$ null **do**
4: Parameters Estimation, $s_i^{RF}(t)$: $\mathbf{\Theta}_i = [f_i^e, \mu_i, T_i]$;
5: $i = i + 1$;
6: **if** $i = 1$ **then**
7: Create the first mode: $\mathbb{M}_1 = \{[s_1^{RF}(t)], [\mathbf{\Theta}_1]\}$;
8: $N_m = N_m + 1$;
9: **else**
10: Compare with existing modes $D(n) = \overline{ED}(\mathbf{\Theta}_i, \mathbb{M}_n\{\mathbf{\Theta}\}), n = 1, 2, \cdots, N_m$;
11: $I^{\min} = \arg\min_n D(n)$, $D^{\min} = D(I^{\min})$;
12: **if** $D^{\min} < \gamma$ **then**
13: Assign $s_i^{RF}(t)$ and $\mathbf{\Theta}_i$ into mode $\mathbb{M}_{I^{\min}}$.
14: **else**
15: Create a new mode: $\mathbb{M}_{N_m+1} = \{[s_i^{RF}(t)], [\mathbf{\Theta}_i]\}$;
16: $N_m = N_m + 1$;
17: **end if**
18: **end if**
19: **if** i mod N_w == 0 **then**
20: break;
21: **end if**
22: **end while**
{*Library Refinement*}
23: **for** $n = 1 : N_m$ **do**
24: **if** pulse number of $\mathbb{M}_n \leq \lambda$ **then**
25: Delete mode $\mathbb{M}_n$ from the library $\mathbb{L}$;
26: $N_m = N_m - 1$;
27: **end if**
28: **end for**
29: **return** $\mathbb{L} = [\mathbb{M}_1, \mathbb{M}_2, \cdots, \mathbb{M}_{N_m}]$.

where γ_m represent the minimum distance between all target modes (the modes expected to be classified) and γ_p is the maximum difference between the pulse signals within the same target mode caused by RFFs, calculation errors and other factors.

C. Library Self-Refinement

There may be interference pulses, caused by pulse superposition, pulse truncation, complex electromagnetic environment effects, etc. They should be assigned to interference modes, which brings a negative impact to radar identification. The library is thus self-refined whenever the observation window ends by clearing the operation modes whose pulses number are less than the threshold of deleting interference pulse mode, λ.

The length of observation window N_w and the threshold λ are two related parameters, which should satisfy

$$P_I < \frac{\lambda}{N_w} < P_T, \tag{13}$$

where P_I indicates the proportion of the maximum pulse number of the interference modes (the operation modes consist of interference pulses) in the total pulse number, P_T indicates the proportion of the minimum pulse number of the target modes in the total pulse number.

Finally, we define three parameters, the ratio of correctly classified target pulse R_T, the ratio of correctly deleted interference pulses R_I and the number of modes that ultimately exist in the library N_L, to evaluate the performance of this algorithm. The ideal values of them are $R_T = 100\%$, $R_I = 100\%$ and N_L equals the number of target modes.

For other types of radars, the proposed DRC algorithm is also applicable, as long as the parameters set $\mathbf{\Theta}$ is replaced by the modulation parameters corresponding to the input pulses.

V. Denoising using PCFD

RFF identification is sensitive to noise because severe noise will submerge RFF features. Hence, it is necessary to reduce the noise effect of the received pulse before RFF extraction. We propose a denoising algorithm for LFM pulses based on piecewise curve fitting, named PCFD, which consists of two parts, signal preprocessing and piecewise curve fitting.

A. Signal Preprocessing

The pulse signal $S^{RF}(t)$ is down-converted with respect to frequency f^e that is estimated in the DRC algorithm. The process can be given as

$$\begin{aligned} s(t) =& s^{RF}(t)\exp(-j2\pi f^e t) \\ =& \exp(j2\pi(\Delta f + 0.5\mu t)t + \varphi) + Z(t), \\ =& \exp(j\xi(t)t + \varphi) + Z(t) \\ & 0 \le t \le T, \end{aligned} \tag{14}$$

where $\Delta f = f_F + f_F^c + f^\delta$ represents the frequency offset and $f^\delta = f^e - (f_0^c + f_0)$ is the estimation error, $Z(t)$ is the noise after digital down-conversion, which is still the AWGN with zero mean and variance σ^2, and

$$\xi(t) = 2\pi(\Delta f + 0.5\mu t), \tag{15}$$

which contains all frequency related RFF features, including f_F, f_F^c in Δf and μ_F in μ.

We then consider the in-phase component of $s(t)$ as the example. The sampled version can be given as

$$\begin{aligned} y(t_n) =& \cos\left(\xi(t_n)t_n + \varphi\right) + z(t_n) \\ n =& 1, 2, \cdots, \lfloor T f^s \rfloor, \end{aligned} \tag{16}$$

where f^s is the sampling frequency, $t_n = n f_s$, $z(t_n)$ is the in-phase component of $Z(t)$, and $\lfloor \cdot \rfloor$ represent the floor function.

Algorithm 2 PCFD Algorithm

Input:
$y(t_n)$, LFM pulse signal;
Δf, Estimated frequency offset;
μ, Chirp rate;
f_s, Sampling frequency.

Output:
$y^f(t_n)$, The fitted signal.

{*Initialization*}

1: Initialize the piece number $k = 0$;
2: Initialize the length of signal that has been fitted, $l_k = 0$;
3: $N_y = \text{length}(y(t_n))$;
4: Set $N_0^p = 0$;

{*Signal fitting*}

5: **while** $l_k \le N_y$ **do**
6: $k = k + 1$;
7: $l_k = \sum_{i=0}^{k-1} N_i^p$;
8: $f_k^p = \Delta f + 0.5\mu t_{l_k}$;
9: $N_k^p = f_s / f_k^p$;
10: Get one piece signal of $y(t_n)$, $y_k(t_n) = \cos\left(\xi(t_n)t_n + \varphi\right) + z_k(t_n)$, $n = l_k + 1, l_k + 2, \cdots, l_k + N_k^p$;
11: Get the fitted signal $y_k^f(t_n)$ of $y_k(t_n)$;
12: **end while**
13: **return** the completed fitted signal $y^f = [y_1^f, y_2^f, \cdots, y_K^f]$.

B. Piecewise Curve Fitting

The signal $y(t_n)$ is firstly split into multiple pieces based on the signal waveform period. Each piece is then fitted with reference to the three parameter sine wave curvefit algorithm [33]. The detailed process is explained in Algorithm 2.

The piecewise process is illustrated in Fig. 3. The signal $y(t_n)$ is divided into K pieces, namely $[y_1, y_2, \cdots, y_k, \cdots, y_K]$. The k-th piece signal $y_k(t_n)$ is expressed as

$$\begin{aligned} y_k(t_n) = \cos\left(\xi(t_n)t_n + \varphi_k^p\right) + z_k(t_n), \\ n = l_k + 1, l_k + 2, \cdots, l_k + N_k^p, \end{aligned} \tag{17}$$

where

$$N_k^p = f^s / f_k^p \tag{18}$$

represents the signal length of the k-th signal piece,

$$f_k^p = \Delta f + 0.5\mu t_{l_k} \tag{19}$$

refers to the frequency of the start point of the piece signal, and φ_k^p is the initial phase of this signal piece,

$$l_k = \sum_{i=0}^{k-1} N_i^p, N_0^p = 0 \tag{20}$$

indicates the length of the previous $k-1$ signal pieces.

Then, we start the process of fitting signal $y_k(t_n)$, as shown in line 11. Each piece signal contains one waveform period, which has only a small frequency variation, it can thus be approximated as a sine wave signal. Therefore, according to

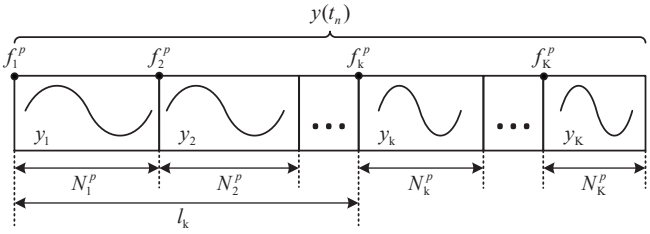

Fig. 3. The schematic diagram of the signal piecewise ($y(t_n)$ is LFM signal, y_k is the k-th piece signal, f_k^p is the frequency of the start point of y_k, and N_k^p is the length of y_k).

the three parameter sine wave curvefit algorithm in [33], the fitted solution of the k-th piece can be written as

$$\begin{aligned} y_k^f(t_n) =& \mathcal{A}\cos\left(\xi\left(t_n\right)t_n+\theta\right)+C \\ =& A\alpha\left(t_n\right)+B\beta\left(t_n\right)+C, \\ \mathcal{A} =& \sqrt{A^2+B^2}, \\ \theta =& \begin{cases} \tan^{-1}\left(\frac{-B}{A}\right) & \text{if } A\geq 0 \\ \tan^{-1}\left(\frac{-B}{A}\right)+\pi & \text{if } A<0 \end{cases} \\ n =& l_k+1, l_k+2, , \cdots, l_k+N_p^k, \end{aligned} \tag{21}$$

where $\alpha\left(t_n\right)=\cos\left(\xi\left(t_n\right)t_n\right)$, $\beta\left(t_n\right)=\sin\left(\xi\left(t_n\right)t_n\right)$. $\xi(t_n)$ can be obtained based on the frequency offset Δf and the chirp rate μ estimated by the FrFT algorithms [50].

A, B, C are the variables to be determined during the fitting process. Then we search for the suitable set of A_k, B_k, C_k to minimize the sum of squared residuals as below [33]

$$A_k, B_k, C_k = \underset{A,B,C}{\arg\min} \sum_{n=l_k+1}^{l_k+N_k^p} \left[y_k(t_n)-y_k^f(t_n)\right]^2. \tag{22}$$

Finally, A_k, B_k, C_k are calculated as

$$A_k=\frac{A_N}{A_D},\ B_k=\frac{B_N}{B_D},\ C_k=\overline{y_k}-A_k\overline{\alpha}-B_k\overline{\beta}, \tag{23}$$

where

$$\begin{aligned} A_N=&\frac{w_7-\overline{y_k}w_2}{w_4-\overline{\beta}w_2}-\frac{w_8-\overline{y_k}w_3}{w_6-\overline{\beta}w_3}, A_D=\frac{w_5-\overline{\alpha}w_2}{w_4-\overline{\beta}w_2}-\frac{w_4-\overline{\alpha}w_3}{w_6-\overline{\beta}w_3}, \\ B_N=&\frac{w_7-\overline{y_k}w_2}{w_5-\overline{\alpha}w_2}-\frac{w_8-\overline{y_k}w_3}{w_4-\overline{\alpha}w_3}, B_D=\frac{w_4-\overline{\beta}w_2}{w_5-\overline{\alpha}w_2}-\frac{w_6-\overline{\beta}w_3}{w_4-\overline{\alpha}w_3}, \\ \overline{y_k}=&\frac{1}{N_k^p}w_1, \qquad \overline{\alpha}=\frac{1}{N_k^p}w_2, \qquad \overline{\beta}=\frac{1}{N_k^p}w_3 \end{aligned} \tag{24}$$

and

$$\begin{aligned} w_1=&\sum_{n=l_k+1}^{l_k+N_k^p} y_k(t_n), & w_2=&\sum_{n=l_k+1}^{l_k+N_k^p} \alpha(t_n), \\ w_3=&\sum_{n=l_k+1}^{l_k+N_k^p} \beta(t_n), & w_4=&\sum_{n=l_k+1}^{l_k+N_k^p} \alpha(t_n)\beta(t_n), \\ w_5=&\sum_{n=l_k+1}^{l_k+N_k^p} \alpha(t_n)^2, & w_6=&\sum_{n=l_k+1}^{l_k+N_k^p} \beta(t_n)^2, \\ w_7=&\sum_{n=l_k+1}^{l_k+N_k^p} y_k(t_n)\alpha(t_n), & w_8=&\sum_{n=l_k+1}^{l_k+N_k^p} y_k(t_n)\beta(t_n). \end{aligned} \tag{25}$$

The fitted signal of $y_k(t_n)$ can be written as

$$\begin{aligned} y_k^f(t_n) &= \mathcal{A}_k\cos\left(\xi(t_n)t_n+\theta_k\right)+C_k, \\ \mathcal{A}_k &= \sqrt{A_k^2+B_k^2}, \\ \theta_k &= \begin{cases} \tan^{-1}\left(\frac{-B_k}{A_k}\right) & if A_k\geq 0 \\ \tan\left(\frac{-B_k}{A_k}\right)+\pi & if A_k<0, \end{cases} \end{aligned} \tag{26}$$

When the fitting results are accurate, $\mathcal{A}_k\approx 1$, $\theta_k\approx\varphi_k^p$ and C_k equal to the mean of $z_k(t_n)$. Theoretically, the mean of an AWGN is zero. However, $z_k(t_n)$ in one signal piece is not a standard AWGN and there may be some noise left, especially when the original signal has low SNR. Thus, we have

$$y_k^f(t_n)=\cos\left(\xi(t_n)t_n+\varphi\right)+\overline{z_k}(t_n), \tag{27}$$

where $\overline{z_k}(t_n)$ represent the residual noise.

Each signal piece will be fitted by the above process. The complete fitted signals can be obtained by concatenating all the fitted signals y_k^f as

$$\begin{aligned} y^f(t_n)=[y_1^f, y_2^f, \cdots, y_K^f] \approx \cos\left(\xi(t_n)t_n+\varphi\right)+z^c(t_n), \\ n=1,2,\cdots,\lfloor Tf_s\rfloor, \end{aligned} \tag{28}$$

where $z^c(t_n)$ represents the residual noise caused by the mean of the noise, $\overline{z_k}(t_n)$, in each signal piece, which is much smaller than the original noise. The RFF features, including f_F, μ_F, f_F^c and T_F in fitted signal $y^f(t_n)$, remain unchanged compared with the original signal $y(t_n)$.

VI. Hybrid RFF identification

This section presents a hybrid RFF identification algorithm, which is divided into three steps, namely signal transformation, RFF feature extraction, and identification.

A. Signal Transformation

We designed a signal transformation to make RFF features more prominent and easy to extract. Both the original and fitted signals are processed for the sake of comparison.

Firstly, the derivative of the fitted signal can be given as

$$\begin{aligned} y^{f\prime}(t_n) =& \frac{\mathrm{d}y^f(t_n)}{\mathrm{d}t_n} \\ \approx& -\sin\left(2\pi(\Delta f+0.5\mu t_n)t_n+\varphi\right) \\ & \times\left(2\pi(\Delta f+\mu t_n)\right)+z^{c\prime}(t_n), \end{aligned} \tag{29}$$

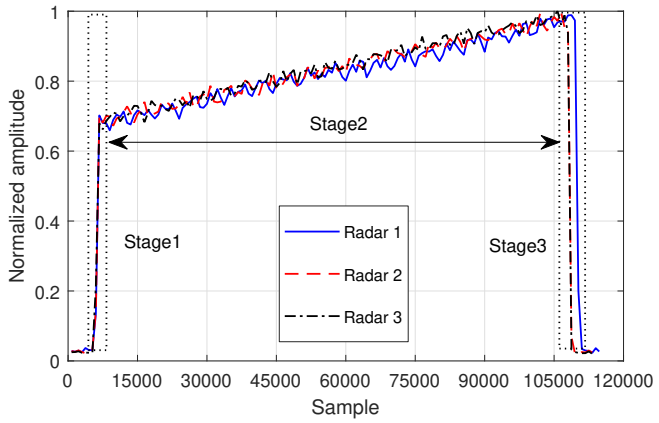

Fig. 4. The envelopes of the derivatives of the pulses, $\widetilde{y'}(t_n)$, from three radars.

where $z^{c\prime}(t_n)$ represents the derivative of $z^c(t_n)$. The derivative of signal $y(t_n)$ can be written as

$$\begin{aligned} y'(t_n) =& \frac{\mathrm{d}y(t_n)}{\mathrm{d}t_n} \\ =& -\sin\left(2\pi(\Delta f + 0.5\mu t_n)t_n + \varphi\right) \\ & \times \left(2\pi(\Delta f + \mu t_n)\right) + z'(t_n), \end{aligned} \tag{30}$$

where $z'(t_n)$ is the derivative of $z(t_n)$.

We then obtained the envelopes of $y^{f\prime}(t_n)$ and $y'(t_n)$ by Hilbert transform [51] ($\mathcal{H}[\cdot]$), which can be given as

$$\widetilde{y^{f\prime}}(t_n) = |y^{f\prime}(t_n) + j\mathcal{H}[y^{f\prime}(t_n)]|, \tag{31}$$

$$\widetilde{y'}(t_n) = |y(t_n) + j\mathcal{H}[y(t_n)]|. \tag{32}$$

When ignoring the interference of the noise, the theoretical expression of the envelope signals, $\widetilde{y^{f\prime}}(t_n)$ and $\widetilde{y}(t_n)$ are calculated as

$$\Gamma(t_n) = 2\pi(\Delta f + \mu t_n), n = 1, 2, \cdots, \lfloor T f_s \rfloor. \tag{33}$$

The RFF features related parameters, $\Delta f, \mu, T$, studied in this paper correspond to the parameters of $\Gamma(t_n)$. The frequency offset, chirp rate and pulse width corresponds to the y-intercept, slope, and length of $\Gamma(t_n)$, respectively.

Finally, since this paper focuses on the trend of envelope signals $\widetilde{y^{f\prime}}(t_n)$ and $\widetilde{y'}(t_n)$, the moving average are used to further reduce the effects of signal glitch and the normalization is used to eliminate the effects of received signal power change.

B. RFF Feature Extraction

Fig. 4 illustrates an example of the envelops of the actual pulses' derivatives, $\widetilde{y'}(t_n)$, from three radars operating at Mode 1. There are differences in the slope and length of the three curves, which is consistent with the above analysis about the RFF in (33). In addition, it shows that the envelopes signal can be divided into 3 stages.

- Stage 1 refers to the radar turn-on transient when the signal power rises from zero to the rated power.
- Stage 2 refers to the radar's stable operation period when the signal is maintained at a rated power.
- Stage 3 refers to the radar turn-off transient when the signal power drops from the rated power to zero.

The midpoints of stages 1 and 3 are the arrival time of pulse rising edge, t_i^1, and pulse falling edge t_i^2, respectively, which have been calculated in (9). After setting a suitable interval width, stages 1 and 3 can be extracted conveniently. Then, the rest of the pulse is stage 2.

The signals of stages 1 and 3 are the transient signals, which contain the transient-based RFFs of the radar emitter. Since transient signals are difficult to express with mathematical formulas, the distortion caused by hardware imperfections on transient signals (transient-based RFF) is difficult to be theoretically expressed. However, transient-based RFF can be effectively reflected by the transient signal envelope [25], [44]. To further prove this point of view, we exemplifies the stage 1 and stage 3 of the envelopes of the pulses' derivatives in Fig. 5. It can be seen that the envelopes of three pulses of each radar have the same trend of change. However, there are clear differences among different radars in both stage 1 and stage 3, especially the steepness of the rise or fall. Therefore, we sampled the envelope of the stage 1 and get $\mathbf{F}_T^r = [p_1^r, p_2^r, \cdots, p_{N_1}^r]$, and sampled the envelope of the stage 3 and get $\mathbf{F}_T^d = [p_1^d, p_2^d, \cdots, p_{N_3}^d]$. The transient-based RFF features, $\mathbf{F}_T$, are thus constructed as

$$\mathbf{F}_T = [\mathbf{F}_T^r, \mathbf{F}_T^d]. \tag{34}$$

Stage 2 is the steady-state signal that contains the RFFs of frequency offset, chirp rate and pulse width, as analyzed in (33). We divided the envelope signal in stage 2 evenly into multiple slices, i.e., $\{\eta_i\}, i = 1, 2, ..., N_2$. The modulation-based RFF features, $\mathbf{F}_M$, are composed of the expectations of the slices, give as

$$\mathbf{F}_M = [E(\eta_1), E(\eta_2), \cdots, E(\eta_{N_2})], \tag{35}$$

where $E(\cdot)$ indicates the expectation operation.

Finally, the hybrid RFF features vector $\mathbf{F}$ is given as

$$\mathbf{F} = [\mathbf{F}_T, \mathbf{F}_M] \tag{36}$$

C. RFF Identification

RFF identification usually involves a training stage and an identification stage. During the training stage, the RFF feature library is established by obtaining reference RFF features, $\mathbf{F}_{ref}$, from verified radars. Since the RFF feature is related to the signal form, we need to build the RFF feature libraries for each operation modes. Then, in the identification stage, pulses with different operation modes should be identified with the corresponding RFF feature library.

The identification is carried out by calculating the minimum Mahalanobis distance ($MH(\cdot,\cdot)$) between the reference RFF features in the library and the RFF features of the received LFM signals, which can be given as

$$L^r = \arg\min_L MH\big(\mathbf{F}_{ref}(L), \mathbf{F}(L^t)\big), \tag{37}$$

where L is the radar label of the pulses in the library, L^t is the true radar label of the received LFM pulse to be identified (it is not known in practical applications, but is known in the

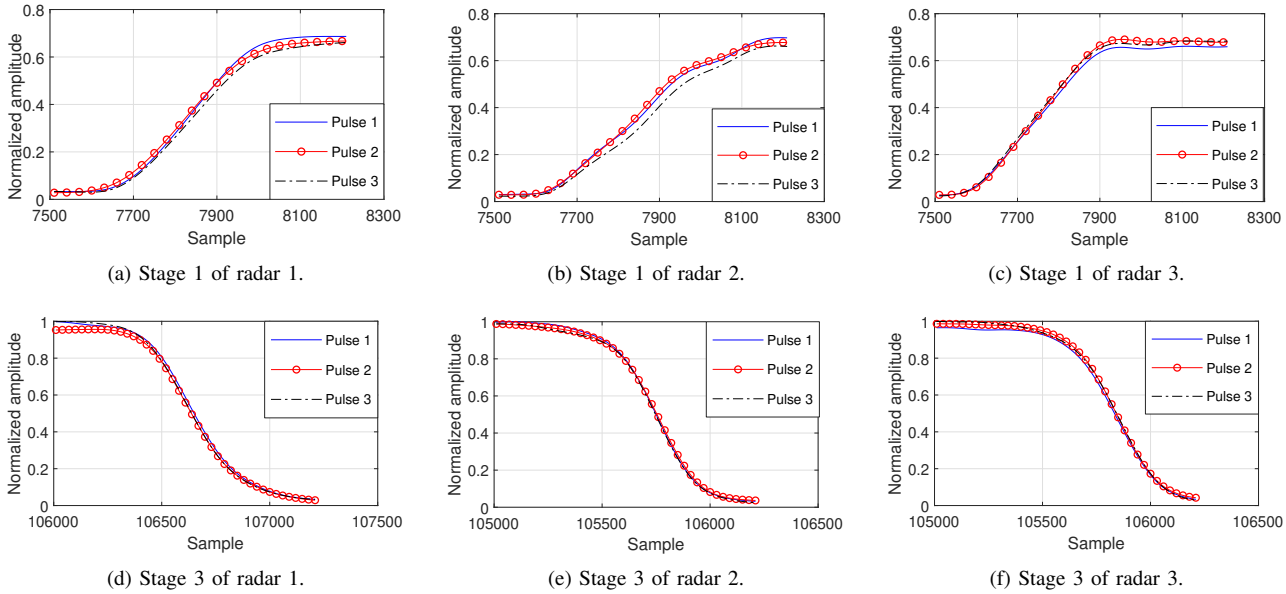

(a) Stage 1 of radar 1. (b) Stage 1 of radar 2. (c) Stage 1 of radar 3.

(d) Stage 3 of radar 1. (e) Stage 3 of radar 2. (f) Stage 3 of radar 3.

Fig. 5. Comparsion of the envelopes of the pulses' derivatives, $\widetilde{y}'(t_n)$, from three radars in stage 1 and stage 3.

experiment for evaluating algorithm performance) and L^r is the result. When $L^t = L^r$ and the Mahalanobis distance is less than the threshold D_{th},

$$MH\big(\mathbf{F}_{ref}(L^r), \mathbf{F}(L^t)\big) < D_{th}, \tag{38}$$

the identification is correct. Otherwise, there is a wrong identification when $L^t \neq L^r$ or L^t is identified as a rogue device when distance is greater than the threshold D_{th}.

Here, we define the identification accuracy rate ζ as

$$\zeta = \frac{N_T}{N_{All}} \tag{39}$$

where N_{All} is the number of received pulses and N_T is the number of correctly identified pulses.

VII. Performance Evaluation

A. Radar Data-sets

We investigated LFM pulses from three real radars (same model with different serial number), $N_R = 3$; each pulse may operate at one of the four modes, $N_M = 4$, listed in Table I. We collected 2,000 pulses from each mode of each radar; hence, we collected $N_S = 2,000 * 3 * 4 = 24,000$ pulses in total. The collected pulses are signals directly transmitted by the target radar rather than reflected signals Oversampling rate is 2.5 times the maximum frequency of the LFM pulses.

1) Artificial Interference Pulse: Since there were no interference pulses in the collected datasets, we deliberately added some interference pulses in the mode classification experiments to evaluate the anti-interference ability of our DRC algorithm. We randomly selected 2,400 pulses from the datasets and generated interference pulses by cutting them off, superimposing them or changing their parameters, etc., for the purpose of emulating different types of interference pulses. Finally, the raw dataset and the artificially generated interference pulses were randomly shuffled. The entire dataset then would have 26,400 pulses.

2) Additive Noise: For the RFF identification experiments, 500 pulses from each radar were used for training and the remaining 1,500 pulses from each radar were test set. Since the original dataset was obtained under high SNR conditions, additive white Gaussian noise (AWGN) was added by MATLAB to evaluate the noise effect. We used MATLAB-SNR (MANR) to represent the level of the added AWGN in this paper, which is defined as the power of the received signal to that of the added AWGN. In the experiment, the MSNR was set as {-15, -10, -5, ... , 20, 25} dB.

3) Parameters Setting: There are three parameters in DRC algorithm that need to be set. The first is the distance threshold of mode classification, γ, which should satisfy $\gamma_p < \gamma < \gamma_m$ in (12). Next are two related parameters in (13), the length of observation window N_w and the threshold of deleting interference pulse mode λ. However, in the absence of prior information, the upper and lower bounds of γ and $\frac{\lambda}{N_w}$ are generally not available in practical applications. They need to be estimated based on the statistical characteristics of the received pulses. In this paper, the γ was configured as an empirical values, $\gamma = 0.1$, the N_w was fix as $N_w = 500$, and λ was changed in the interval of [1, 120] with the step of 1 to analyze the impact of $\frac{\lambda}{N_w}$ on mode classification.

B. Performance of Operation Mode Classification Using DRC

The purpose of the DRC algorithm is to accurately classify the four target operation modes with the randomly shuffled input pulses and effectively remove all interference pulses.

Fig. 6 shows the impact of the threshold λ on the ratio of correctly classified target pulse R_T, the ratio of correctly deleted interference pulses R_I and the number of modes that ultimately exist in the library N_L.

- When $1 \leq \lambda < 8$, R_T is stable at 100%, R_I goes from 0 to 100%, N_L is more than 4. This phenomenon means the target pulses (pulses belonging to the target operation

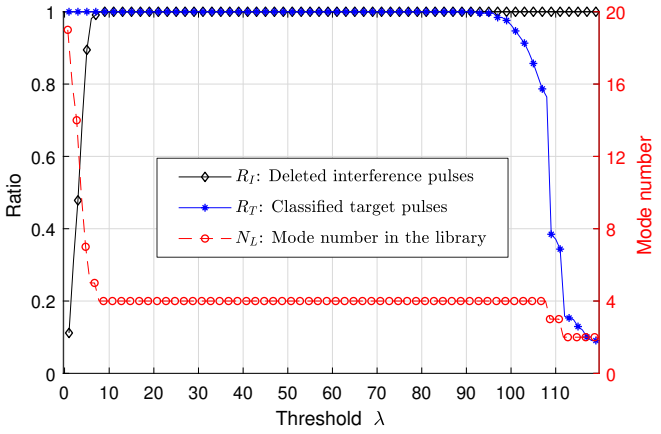

Fig. 6. Impact of the threshold, λ, on mode classification results.

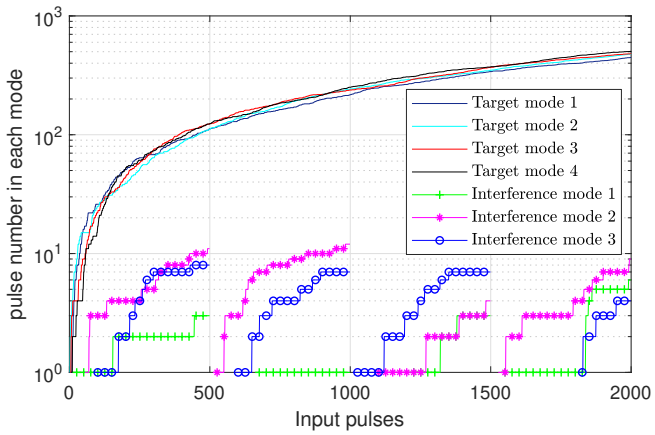

Fig. 7. The dynamic process of library self-refinement.

modes) are all correctly classified. However, the interference pulses are not cleaned up as many interference pulses are wrongly judged as target pulses and pushed into a new mode.

- When $91 < \lambda \leq 120$, R_T decreases rapidly from 100% to 9.08%, R_I is stable at 100% and N_L goes from 4 to 2. It is because that the interference pulses are cleaned up while some target pulses are deleted incorrectly.
- Only in the interval of $8 \leq \lambda \leq 91$, these parameters, R_T, R_I and N_L, are stable at ideal values, which points out that the values of λ in this interval are reasonable.

In this paper, most artificial interference pulses have a large distance, so maximum number of pulses in the interference mode is considered to be less than 100. Then, according to that the minimum pulse number of the target modes is 6,000 and total pulses number is 26,400, (13) can be written as $\frac{100}{26400} < \frac{\lambda}{N_w} < \frac{6000}{26400}$, which is $4 < \lambda < 113$. Experimental results are basically consistent with this theoretical result. One reason for the small difference between them may be that the input pulses were not completely randomly shuffled within an observation window. Therefore, in the practical applications, the setting of the λ needs to take into account that the left and right limits of the theoretical interval may move toward the middle.

Fig. 7 shows the performance of the dynamic process of refining operation mode library. The target mode represents the operation mode consisting of the pulses to be identified, and the interference mode means the mode caused by the interference pulses (for clarity, only three interference modes are shown in this figure). In the beginning, when input pulse is 0, there is no existing mode in the library. As the input pulses arrives, the pulse will be assigned to an existing mode or be created as a new mode. Whenever the number of input pulses is an integer multiple of the observation window (500 in this paper), the algorithm refines the library by comparing the pulse number of each existing mode and the threshold λ. Take the interval [0, 500] as an example, the pulse number of target mode and interference mode increases as the input pulse arrives within the observation window. When the number of input pulses is 500, all interference mode are cleared while the target mode continues to grow.

C. Performance of Denoising Using PCFD

Fig. 8 presents the fitting and denoising effect of the PCFD algorithm when it is applied to the pulses. In order to show the denoising performance, we deliberately created a noisy version of the original signal $y(t_n)$ by adding a 5 dB noise. We then carried out the PCFD algorithm to the noisy signal. As can be observed in Fig. 8, the fitted signal is very smooth compared to the noisy signal, which means that noise suppression is effective. In addition, the original signal and the fitted signal match well for the entire pulse, which demonstrates that the signal fitting does not destroy the information in the original signal. The presence of some glitches, e.g., in Fig. 8c, reflects the existence of residual noise, which however only has a very small effect on the fitted signal.

Fig. 9 further shows the fitting effect by comparing the envelopes of the derivatives of the original signal and the fitted signal, $\widetilde{y'}(t_n)$ and $\widetilde{y^{f'}}(t_n)$. They are almost identical in all stages, which indicates that the PCFD algorithm does not destroy the RFF information of the original pulse.

Fig. 10 demonstrates the denoising performance of the PCFD algorithm. The envelope of the actual pulse's derivative is gradually overwhelmed by noise. In particular, when MSNR = 10 dB, the rising and falling stages of the envelope are hard to be detected and the curve in the modulation stage also has severe burrs. It is thus very difficult to extract the RFF features accurately in such a bad condition. Therefore, denoising is necessary to be performed before the RFF extraction. Regarding the envelopes after the PCFD algorithm, the fitted signals, $\widetilde{y^{f'}}(t_n)$, match well with the original signal when MSNR is above 0 dB. Therefore, the RFF features extracted from the fitted signals under different MSNR are almost identical. In other words, the RFF library established under an appropriate SNR can be applied to different SNR scenarios. When the MSNR is 0 dB the envelope changes a lot because the residual noise of the fitted pulse, $z^c(t_n)$, significantly increases, and thus the RFF information is also damaged.

D. Performance of RFF Identification

Fig. 11 shows the identification performance under different modes using hybrid RFF. We also compared the performance

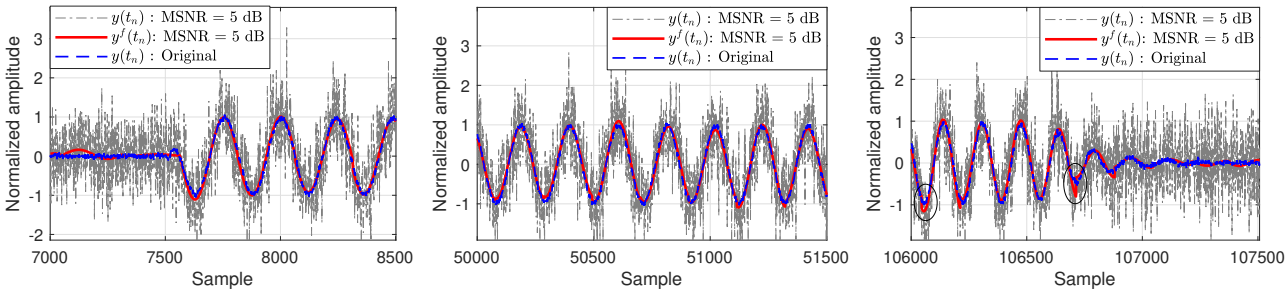

(a) The beginning of the pulse. (b) The middle of the pulse. (c) The end of the pulse.

Fig. 8. Comparison of the noisy signal $y(t_n)$, 5 dB, the fitted signal $y^f(t_n)$, and the original recorded signal $y(t_n)$.

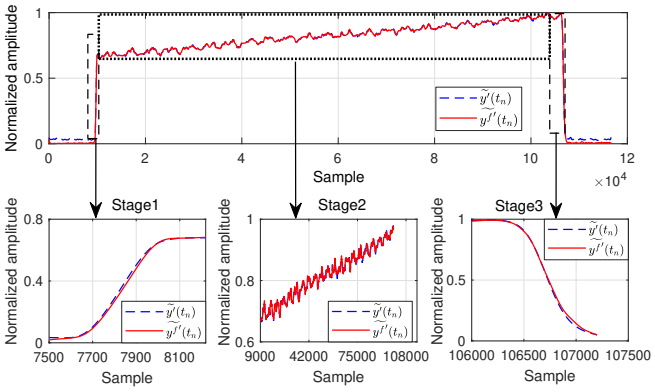

Fig. 9. The envelopes of the derivatives of the recorded signal and the fitted signal, $\widetilde{y'}(t_n)$ and $\widetilde{y^{f'}}(t_n)$.

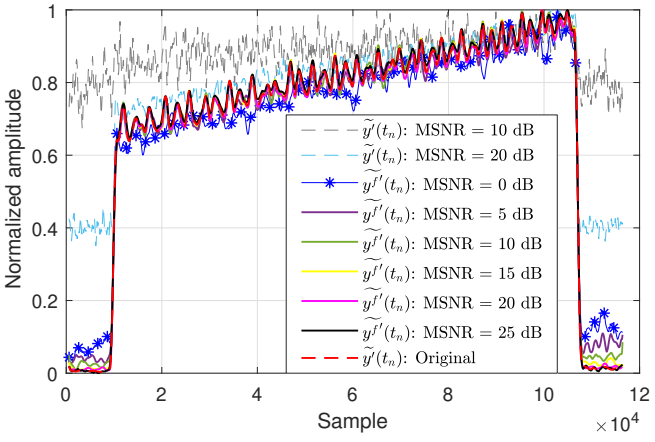

Fig. 10. The envelopes of the fitted pulses' derivatives, $\widetilde{y^{f'}}(t_n)$, at different MSNRs. The envelopes of unfitted signals, $\widetilde{y'}(t_n)$.

for pulses with mixed modes, i.e., without mode classification. We established multiple libraries with different SNR levels, and then selected the corresponding library for the test phase according to the SNR of the received pulse for radar identification. In this way, we maintained the same SNR between the train and test pulses. As can be calculated from Table I, the bandwidth of Mode 3 and Mode 4 is 4 MHz while the bandwidth of Mode 1 and Mode 2 is 2 MHz. It can be seen that our RFF-based radar identification scheme works well in four

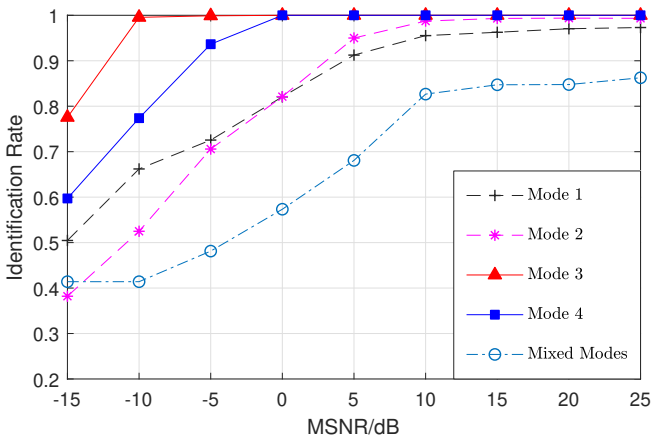

Fig. 11. The identification rates of different modes at MSNRs from -15 dB to 25 dB.

operation modes when the pulses were classified into different modes. Mode 3 and Mode 4 maintain a 100% identification rate when MSNR $\geq$ 0 dB. Because Mode 1 and Mode 2 has a smaller bandwidth than that of Mode 3 and Mode 4, the overall identification performance of them are not as good as that of Modes 3 and Mode 4. The larger bandwidth of the pulse, the wider working range of the device hardware component. In contrast, the identification rate without mode classification is not ideal in all SNR scenarios. Therefore, it could be concluded that the mode classification is necessary and our proposed radar identification scheme is useful for multi-mode radar identification.

Fig. 12 presents the identification rates when using different RFF features, taking Mode 4 as an example. Both transient-based ($\mathbf{F}_T$) and modulation-based RFF ($\mathbf{F}_M$) behave well while the hybrid RFF ($\mathbf{F}$) identification performs best. Even if the MSNR is as low as 0 dB, the identification accuracy is 100%. However, when the PCFD algorithm is not applied, i.e., the pulses are affected by noise, the identification rate is quite low, because the noise overwhelms RFF information at low SNR. In addition, the derivative operation amplifies noise effect, and further blurs the small RFF features. The comparison shows that our proposed PCFD algorithm performs well in denoising without destroying RFF features.

Fig. 13 shows the identification rate of four modes when the MSNR of the library is 20 dB, but the MSNR of the test data

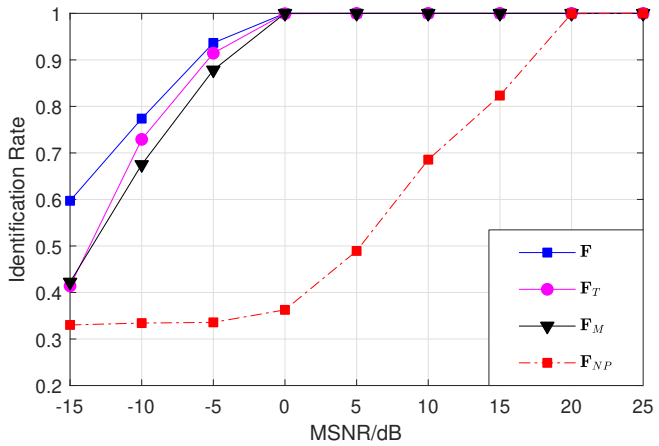

Fig. 12. The identification rates of different RFF features used at MSNRs from -15 dB to 25 dB. ($\mathbf{F}$: hybrid RFF, $\mathbf{F}_T$: transient-based RFF, $\mathbf{F}_M$: modulation-based RFF, $\mathbf{F}_{NP}$: hybrid RFF without PCFD algorithm).

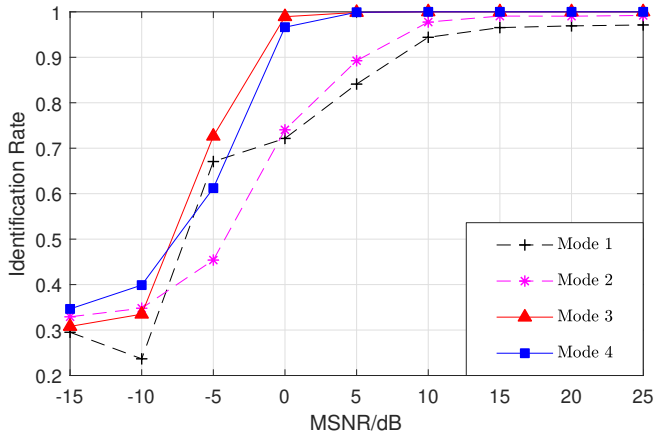

Fig. 13. The identification rates of different modes at MSNRs from -15 dB to 25 dB, when the MSNR of library is 20 dB.

is changing from -15 dB to 25 dB. The hybrid RFF features and PCFD algorithm are used in this experiment. The overall identification performance is not as good as that in Fig. 11. However, it also has an acceptable identification accuracy (higher than 95%) in high SNR (MSNR $\geq$ 10 dB) scenarios. The results suggest that the radar RFF library constructed at the appropriate SNR can meet the identification requirements in various SNR scenarios. This is a significant advantage for practical engineering applications, as it is not easy to build a radar RFF library containing all SNR scenarios in an actual radar identification application.

Table II compares our results with the existing methods [17], [21], [47], [52]. Regarding the comparison with the methods focusing on single mode radar identification [21], [47], [52], our scheme obtains the same greatest identification rate, $\zeta = 100\%$ in high SNR scenarios and a superior performance when SNR is low. For the research of LFM signals in [21], its identification accuracy decreases to 52% when MSNR = 6 dB, while our Mode 3 maintains at 100% even when MSNR = -5 dB, and declines to approximately 77.6% until MSNR drops to -15 dB. By contrast with the studies on real radar data in [47] and [52], our scheme shows better performance with the same number of radars, a larger sample set, and lower SNR. Our method achieves the same best identification rate, $\zeta = 100\%$, even when MSNR = -5 dB. Regarding the research of multi-mode radar, [17] only studied the classification of two radars with three modes (20 pulses per mode). Their work does not give clear classification data. Therefore, we estimate its recognition rate according to its RFF feature distribution figures. Comparing with it, our scheme behaves well in both the best performance mode (Mode 3) and the worst performance mode (Mode 1). However, considering the factors of the radar number, samples size and SNR, the comprehensive performance of our paper is superior to it. In conclusion, big sample size collected from real muli-mode radars and excellent accuracy suggest that our scheme are more meaningful for practical applications.

VIII. Conclusion

This paper designed a robust RFF-based identification scheme for multi-mode LFM radar. Firstly, a DRC algorithm was proposed to classify pulses into different operation modes since RFF features are always related to the signal form. Then, we presented a denoising algorithm, PCFD, which is effective for noise suppression without disrupting RFF features. Finally, we have addressed the problem of RFF-based radar identification based on both transient-based and modulation-based RFF features extracted from the envelope of the derivative of the signal. A minimum Mahalanobis distance classifier has been used to identify specific radar emitters with the same mode. Experiments based on three real radars operating in four modes with a total of 24,000 pulses demonstrated that our proposed radar identification scheme performs well. Especially, it shows excellent identification accuracy in Mode 3 of which identification rate is almost 100% even when the MSNR is -10 dB. Our future work will further improve the practicality of the scheme by increasing the number of target radars and the complexity of the operation modes. We will also investigate the influence of the multipath channel on radar identification.

References

[1] S. D. Blunt and E. L. Mokole, "Overview of radar waveform diversity," *IEEE Aerosp. Electron. Syst. Mag.*, vol. 31, pp. 2–42, Nov. 2016.

[2] M. Xing, X. Jiang, R. Wu, F. Zhou, and Z. Bao, "Motion compensation for UAV SAR based on raw radar data," *IEEE Trans. Geosci. Remote Sensing*, vol. 47, no. 8, pp. 2870–2883, Aug. 2009.

[3] M. Q. Nguyen, A. Flores-Nigaglioni, and C. Li, "Range-gating technology for millimeter-wave radar remote gesture control in IoT applications," in *Proc. IEEE MTT-S Int. Wireless Symp. (IWS)*, Chengdu, China, May 2018, pp. 1–4.

[4] S. Kuutti, S. Fallah, K. Katsaros, M. Dianati, F. Mccullough, and A. Mouzakitis, "A survey of the state-of-the-art localization techniques and their potentials for autonomous vehicle applications," *IEEE Internet Things J.*, vol. 5, pp. 829–846, Apr. 2018.

[5] Y. Lang, Q. Wang, Y. Yang, C. Hou, H. Liu, and Y. He, "Joint motion classification and person identification via multitask learning for smart homes," *IEEE Internet Things J.*, vol. 6, pp. 9596–9605, Dec. 2019.

[6] E. Cardillo and A. Caddemi, "Feasibility study to preserve the health of an industry 4.0 worker: a radar system for monitoring the Sitting-Time," in *Proc. II Workshop on Metrology for Industry 4.0 and IoT (MetroInd 4.0 IoT)*, Naples, Italy, Jun. 2019, pp. 254–258.

TABLE II
COMPARISON WITH EXISTING WORK. N_R, N_M,N_S INDICATE THE NUMBER OF RADARS, OPERATION MODES AND SAMPLE SIZE, RESPECTIVELY. ζ REPRESENTS THE IDENTIFICATION RATE. * IN THE COLUMN OF MSNR INDICATES THE MEASURED SNR.

Method	Data source	N_R	N_M	N_S	ζ	MSNR	Remark
Świercz [21]	Simulation	5	1	205	100%	Infinite	–
Świercz [21]	Simulation	5	1	205	52%	6 dB	–
Wu *et al.* [52]	Real	3	1	1,000	85.3%	*10 dB	2 signal sources and 1 real radar
Aubry *et al.* [47]	Real	3	1	600	100%	–	–
D'Agostino *et al.* [17]	Real	2	3	60 (20 for each mode)	100%	–	Mode A
					100%	–	Mode B
					<100%	–	Mode C
Ours	Real	3	4	24,000 (6,000 for each mode)	100%	-5 dB	Mode 3
					77.6%	-15 dB	Mode 3
					95.53%	10 dB	Mode 1
					50.5%	-15 dB	Mode 1

[7] Y. Ma, Y. Zeng, and S. Sun, "A software defined radio based multi-function radar for IoT applications," in *Proc. 24th Asia-Pacific Conf. Commun. (APCC)*, Ningbo, China, Nov. 2018, pp. 239–244.

[8] K. Zhang, X. Liang, R. Lu, and X. Shen, "Sybil attacks and their defenses in the internet of things," *IEEE Internet Things J.*, vol. 1, pp. 372–383, Oct. 2014.

[9] Q. Tian, Y. Lin, X. Guo, J. Wen, Y. Fang, J. Rodriguez, and S. Mumtaz, "New security mechanisms of high-reliability IoT communication based on radio frequency fingerprint," *IEEE Internet Things J.*, vol. 6, pp. 7980–7987, Oct. 2019.

[10] Y. H. Hwang, "Iot security & privacy: Threats and challenges," in *Proc. 1st ACM Workshop IoT Privacy, Trust, Secur.*, New York, NY, USA, 2015, pp. 1–1.

[11] J. M. McGinthy, L. J. Wong, and A. J. Michaels, "Groundwork for neural network-based specific emitter identification authentication for iot," *IEEE Internet Things J.*, vol. 6, pp. 6429–6440, Aug. 2019.

[12] N. Vidgren, K. Haataja, J. L. Patiño-Andres, J. J. Ramírez-Sanchis, and P. Toivanen, "Security threats in zigbee-enabled systems: Vulnerability evaluation, practical experiments, countermeasures, and lessons learned," in *Proc. 46th Hawaii Int. Conf. Syst. Sci.*, Wailea, Maui, HI, USA, Jan. 2013, pp. 5132–5138.

[13] J. Sun, G. Xu, W. Ren, and Z. Yan, "Radar emitter classification based on unidimensional convolutional neural network," *IET Radar, Sonar Navig.*, vol. 12, pp. 862–867, Aug. 2018.

[14] S. Guo, R. E. White, and M. Low, "A comparison study of radar emitter identification based on signal transients," in *Proc. IEEE Radar Conf. (RadarConf18)*, Oklahoma City, OK, USA, Apr. 2018, pp. 0286–0291.

[15] B. Danev, D. Zanetti, and S. Capkun, "On physical-layer identification of wireless devices," *ACM Comput. Surv.*, vol. 45, pp. 6:1–6:29, Dec. 2012.

[16] B. Chatterjee, D. Das, S. Maity, and S. Sen, "RF-PUF: Enhancing IoT security through authentication of wireless nodes using in-situ machine learning," *IEEE Internet Things J.*, vol. 6, no. 1, pp. 388–398, Feb. 2019.

[17] S. D'Agostino, G. Foglia, and D. Pistoia, "Specific emitter identification: Analysis on real radar signal data," in *Proc. Eur. Radar Conf. (EuRAD)*, Rome, Italy, Sep. 2009, pp. 242–245.

[18] S. D'Agostino, "Specific emitter identification based on amplitude features," in *Proc. IEEE Int. Conf. Signal Image Process. Appl. (ICSIPA)*, Kuala Lumpur, Malaysia, Oct. 2015, pp. 350–354.

[19] S. Andrews, R. M. Gerdes, and M. Li, "Towards physical layer identification of cognitive radio devices," in *Proc. IEEE Conf. Commun. Net. Secur. (CNS)*, Las Vegas, NV, USA, Oct. 2017, pp. 1–9.

[20] L. J. Wong, W. C. Headley, S. Andrews, R. M. Gerdes, and A. J. Michaels, "Clustering learned CNN features from raw I/Q data for emitter identification," in *Proc. IEEE Mil. Commun. Conf. (MILCOM)*, Los Angeles, CA, USA, Oct. 2018, pp. 26–33.

[21] E. Świercz, "Automatic classification of LFM signals for radar emitter recognition using wavelet decomposition and LVQ classifier," *Acta Physica Polonica, A.*, vol. 119, pp. 488–494, 2011.

[22] H. Patel, M. A. Temple, and B. W. Ramsey, "Comparison of high-end and low-end receivers for RF-DNA fingerprinting," in *Proc. IEEE Mil. Commun. Conf.*, Baltimore, MD, USA, Oct 2014, pp. 24–29.

[23] C. G. Wheeler and D. R. Reising, "Assessment of the impact of CFO on RF-DNA fingerprint classification performance," in *Proc. Int. Conf. Comput. Netw. Commun. (ICNC)*, Santa Clara, CA, USA, Jan. 2017, pp. 110–114.

[24] D. A. Knox and T. Kunz, "AGC-based RF fingerprints in wireless sensor networks for authentication," in *Proc. IEEE Int. Symp. World Wireless Mobile Multimedia Netw. (WoWMoM)*, Montrreal, QC, Canada, Jun. 2010, pp. 1–6.

[25] H. J. Patel, M. A. Temple, and R. O. Baldwin, "Improving ZigBee device network authentication using ensemble decision tree classifiers with radio frequency distinct native attribute fingerprinting," *IEEE Trans. Rel.*, vol. 64, pp. 221–233, Mar. 2015.

[26] Y. Xing, A. Hu, J. Zhang, L. Peng, and G. Li, "On radio frequency fingerprint identification for DSSS systems in low SNR scenarios," *IEEE Commun. Lett.*, vol. 22, pp. 2326–2329, Nov. 2018.

[27] F. Xie, H. Wen, Y. Li, S. Chen, L. Hu, Y. Chen, and H. Song, "Optimized coherent integration-based radio frequency fingerprinting in internet of things," *IEEE Internet Things J.*, vol. 5, no. 5, pp. 3967–3977, Oct. 2018.

[28] J. Yu, A. Hu, F. Zhou, Y. Xing, Y. Yu, G. Li, and L. Peng, "Radio frequency fingerprint identification based on denoising autoencoders," in *Proc. 15th Int. Conf. Wireless Mobile Comput. Netw. Commun. (WiMob)*, Barcelona, Spain, Oct. 2019, pp. 1–6.

[29] L. Peng, A. Hu, J. Zhang, Y. Jiang, J. Yu, and Y. Yan, "Design of a hybrid RF fingerprint extraction and device classification scheme," *IEEE Internet Things J.*, vol. 6, pp. 349–360, Feb. 2019.

[30] S. U. Rehman, K. W. Sowerby, and C. Coghill, "Radio-frequency fingerprinting for mitigating primary user emulation attack in low-end cognitive radios," *IET Commun.*, vol. 8, no. 8, pp. 1274–1284, May 2014.

[31] G. Kim, J. Mun, and J. Lee, "A peer-to-peer interference analysis for automotive chirp sequence radars," *IEEE Trans. Veh. Technol.*, vol. 67, no. 9, pp. 8110–8117, Sep. 2018.

[32] X. Hu, Y. Li, M. Lu, Y. Wang, and X. Yang, "A multi-carrier-frequency random-transmission chirp sequence for TDM MIMO automotive radar," *IEEE Trans. Veh. Technol.*, vol. 68, no. 4, pp. 3672–3685, Apr. 2019.

[33] "IEEE standard for digitizing waveform recorders," *IEEE Std 1057-2017 (Revision of IEEE Std 1057-2007) - Redline*, pp. 1–313, Jan. 2018.

[34] Y. Xing, A. Hu, J. Yu, G. Li, L. Peng, and F. Zhou, "A robust radio frequency fingerprint identification scheme for LFM pulse radars," in *Proc. 15th Int. Conf. Wireless Mobile Comput. Netw. Commun. (WiMob)*, Barcelona, Spain, Oct. 2019, pp. 1–6.

[35] S. Liu, X. Yan, P. Li, X. Hao, and K. Wang, "Radar emitter recognition based on SIFT position and scale features," *IEEE Trans. Circuits Syst. II*, vol. 65, no. 12, pp. 2062–2066, Dec. 2018.

[36] Q. Guo, P. Nan, X. Zhang, Y. Zhao, and J. Wan, "Recognition of radar emitter signals based on SVD and AF main ridge slice," *J. Commun. Netw.*, vol. 17, no. 5, pp. 491–498, Oct. 2015.

[37] X. Zhou, A. Hu, G. Li, L. Peng, Y. Xing, and J. Yu, "Design of a robust RF fingerprint generation and classification scheme for practical device identification," in *Proc. IEEE Conf. Commun. Netw. Secur. (CNS)*, Washington, DC, USA, Jun. 2019, pp. 1–9.

[38] G. Li, J. Yu, Y. Xing, and A. Hu, "Location-invariant physical layer identification approach for WiFi devices," *IEEE Access*, vol. 7, pp. 106 974–106 986, Aug. 2019.

[39] Y. Sharaf Dabbagh and W. Saad, "Authentication of wireless devices in the internet of things: Learning and environmental effects," *IEEE Internet Things J.*, vol. 6, pp. 6692–6705, Aug. 2019.

[40] K. Satyanarayana, M. El-Hajjar, A. A. M. Mourad, and L. Hanzo, "Deep learning aided fingerprint-based beam alignment for mmWave vehicular

communication," *IEEE Trans. Veh. Technol.*, vol. 68, pp. 10 858–10 871, Sep. 2019.

[41] Y. Wang, J. Wang, W. Zhang, J. Yang, and G. Gui, "Deep learning-based cooperative automatic modulation classification method for MIMO systems," *IEEE Trans. Veh. Technol.*, vol. 69, pp. 4575–4579, Feb. 2020.

[42] Y. Wang, M. Liu, J. Yang, and G. Gui, "Data-driven deep learning for automatic modulation recognition in cognitive radios," *IEEE Trans. Veh. Technol.*, vol. 68, pp. 4074–4077, Feb. 2019.

[43] J. Yu, A. Hu, G. Li, and L. Peng, "A robust RF fingerprinting approach using multi-sampling convolutional neural network," *IEEE Internet Things J.*, pp. 1–1, Apr. 2019.

[44] C. K. Dubendorfer, B. W. Ramsey, and M. A. Temple, "An RF-DNA verification process for ZigBee networks," in *Proc. IEEE Mil. Commun. Conf. (MILCOM)*, Orlando, FL, USA, Oct. 2012, pp. 1–6.

[45] X. Dong, S. Cheng, J. Yang, and Y. Zhou, "Radar specific emitter recognition based on DBN feature extraction," *J. Phys.: Conf. Ser.*, vol. 1176, pp. 1–8, Mar. 2019.

[46] G. Huang, Y. Yuan, X. Wang, and Z. Huang, "Specific emitter identification based on nonlinear dynamical characteristics," *Can. J. Electr. Comput. Eng.*, vol. 39, no. 1, pp. 34–41, Jan. 2016.

[47] A. Aubry, A. Bazzoni, V. Carotenuto, A. De Maio, and P. Failla, "Cumulants-based radar specific emitter identification," in *Proc. IEEE Int. Workshop Inf. Forensics Secur.*, Rome, Italy, Nov. 2011, pp. 1–6.

[48] T. Elshabrawy and J. Robert, "Interleaved chirp spreading lora-based modulation," *IEEE Internet Things J.*, vol. 6, pp. 3855–3863, Apr. 2019.

[49] E. Gallimore, E. Terrill, R. Hess, A. Nager, H. Bachelor, and A. Pietruszka, "Integration and evaluation of a next-generation chirp-style sidescan sonar on the REMUS 100," in *Proc. 2018 IEEE/OES Autonomous Underwater Veh. Workshop (AUV)*, Porto, Portugal, Nov. 2018, pp. 1–6.

[50] H. M. Ozaktas and M. A. Kutay, "The fractional Fourier transform," in *Proc. Eur. Control Conf. (ECC)*, Porto, Portugal, Sep. 2001, pp. 1477–1483.

[51] S. L. Hahn, *Hilbert transforms in signal processing*. Boston: Artech House Boston, 1996, vol. 2.

[52] L. Wu, Y. Zhao, M. Feng, F. Y. O. Abdalla, and H. Ullah, "Specific emitter identification using IMF-DNA with a joint feature selection algorithm," *Electronics*, vol. 8, no. 9, pp. 1–16, Aug. 2019.